

A COMPUTATIONAL STOCHASTIC METHODOLOGY FOR THE DESIGN OF RANDOM META-MATERIALS UNDER GEOMETRIC CONSTRAINTS*

IVI C. TSANTILI[†], MIN HYUNG CHO[‡], WEI CAI[§], AND GEORGE EM KARNIADAKIS[¶]

Abstract. We present a computational stochastic methodology for generating and optimizing random meta-material (MM) configurations with nonoverlapping geometric constraints subject to various types of covariances and distributions characterizing the randomness of the MM configurations. The methodology developed consists of three main components: (1) a deterministic solver for electromagnetic scattering from multiple objects, (2) the Karhunen–Loève (K–L) expansion to represent the correlated configurations of the scattering objects, and (3) the multi-element probabilistic collocation method (ME-PCM) to provide flexibility in achieving desired distributions of the MMs. In the current work, we employ random fields from a Spartan family that includes covariance functions with damped oscillatory behavior. The algorithm is applied to study light propagation through random layered heterojunctions and random 3-D MMs. We found that greater transmission and reflection, compared to the uniformly spaced structures, can be achieved for a structure with an oscillatory spacing profile along the propagation direction. Optimized configurations of the heterojunctions and 3-D MMs have been found with larger or smaller transmission coefficients for different wave numbers of the incoming wave and different correlations.

Key words. meta-materials, electromagnetic scattering, stochastic collocation, Karhunen–Loève expansion, Spartan spatial random fields, correlated randomness

AMS subject classifications. 60G60, 62P30, 78M50

DOI. 10.1137/17M1113473

1. Introduction. Meta-materials (MMs), based on meta-atoms of naturally available components, have provided a wide range of new possibilities to design man-made materials with special properties such as negative permittivity and unconventional magnetic response. For example, nanostructured materials such as a meta-surface for solar cell applications provide new opportunities for light management and energy efficiency [19]. Randomly textured rough surfaces have been used as strong light diffusers to achieve efficient light trapping due to broadband and wide angle properties associated with disorders [20, 24]. Recently, it has been shown that structurally correlated random surfaces can also increase light absorption [23].

In this paper, we develop a general computational methodology to model the randomness in nonoverlapping scattering objects, such as meta-atoms in MMs, with

*Submitted to the journal’s Computational Methods in Science and Engineering section January 25, 2017; accepted for publication (in revised form) December 13, 2017; published electronically March 13, 2018.

<http://www.siam.org/journals/sisc/40-2/M111347.html>

Funding: The first author’s work was supported by NSAF grant U1530401 and the Beijing Computational Science Research Center’s computing facilities. The second author’s work was supported by Simons Foundation grant 404499. The third author’s work was supported by U.S. Army Research Office grant W911NF-17-1-0368 and U.S. National Science Foundations grants DMS-1764187 and DMS-1802143.

[†]Algorithms Division, Beijing Computational Science Research Center, Beijing 100193, China (ivi.tsantili@csrc.ac.cn).

[‡]Department of Mathematical Sciences, University of Massachusetts Lowell, Lowell, MA 01854 (MinHyung_Cho@uml.edu).

[§]Corresponding author. Department of Mathematics, Southern Methodist University, Dallas, TX 75275 (cai@smu.edu).

[¶]Division of Applied Mathematics, Brown University, Providence, RI 02912 (George.Karniadakis@brown.edu).

given target probabilistic characteristics. Of interest is how the correlated random position of the meta-atoms affects optical properties such as transmission and reflection coefficients of random structures [6, 24]. To produce the configuration of random nonoverlapping meta-atoms, we first construct continuous random fields (RFs) or refined discrete fields of position fluctuations with a target covariance and distribution. Subsequently, we project the fields onto specific discrete locations to obtain nonoverlapping scattering objects or random layers. The framework of the methodology consists of three main components: (1) a deterministic solver for the simulation of the electromagnetic scattering from multiple objects, (2) the Karhunen–Loève (K–L) expansion [17, 8] to represent the correlated configurations of the scattering objects, and (3) the multi-element probabilistic collocation method (ME-PCM) to provide flexibility in achieving distributions in MMs [7, 29]. In this paper, we employ random functions from a Spartan family [9, 10, 22], which are models inspired by statistical physics and involve adjustable parameters that enable us to control the amplitude, shape, and correlation length of the RFs [14]. This family includes covariance functions with damped oscillatory behavior.

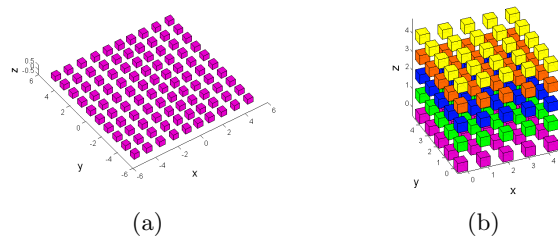


FIG. 1. Sketches of MMs with randomly located cubic meta-atoms in (a) two dimensions and (b) three dimensions.

MMs generated by the proposed methodology are shown in Figure 1. The position of the (randomly) colored meta-atoms can be exploited to affect transmission and reflection coefficients of a multilayered structure for electromagnetic wave propagations. Numerical experiments are presented for different wave numbers of incoming waves, for different correlation lengths, for different types of correlations, and for constant or variable total thickness of the MMs. Also, for randomly located scattering objects within a fixed bounded region, the distribution of the samples generated by this methodology reproduces the so-called clothes-pin entropic force effect [16] that causes the scatterers to cluster near the region's boundaries with a higher probability. Our methodology can be applied for scattering objects of various kinds of MMs and various background materials, characterized by their permittivity and permeability.

The rest of the paper is organized as follows. Section 2 reviews the basic probabilistic techniques for dimensionality reduction in representing random MMs. Section 3 presents the computational framework for generating random MMs with given stochastic properties under nonoverlapping geometric constraints. Then, section 4 introduces the transmission and scattering matrix formulations to compute the transmission and reflection coefficients for multilayered heterojunctions. Section 5 provides a detailed study on the effect of the correlation and clothes-pin entropic force of the distribution on the random heterojunctions. Finally, the conclusion of our study and topics for future work are given in section 6.

2. Stochastic representations of random MMs. In this section, we introduce the components of the computational methodology dealing with the stochastic representation of random MMs.

2.1. Construction of RFs with K–L expansions. Following [22, 8], let (Θ, \mathcal{F}, P) be a probability space and $\mathcal{D} \subseteq \mathbb{R}^d$ the spatial domain of interest. The K–L expansion of an $L^2(\Theta, \mathcal{F}, P)$, centered RF $X(\mathbf{s}, \theta) : \Theta \times \mathcal{D} \rightarrow \mathbb{R}$ with covariance $C(\mathbf{s}_1, \mathbf{s}_2)$ is given by the following superposition of countable sequences of orthonormal eigenfunctions $f_m(\mathbf{s})$ and corresponding eigenvalues $\lambda_m > 0$ that converges uniformly on \mathcal{D} :

$$(1) \quad X(\mathbf{s}, \theta) = \sum_{m=1}^{\infty} \sqrt{\lambda_m} c_m(\theta) f_m(\mathbf{s}),$$

where $f_m(\mathbf{s}_1)$, λ_m are obtained by the solution of the homogeneous Fredholm integral equation of the second kind:

$$(2) \quad \int_{\mathcal{D}} d\mathbf{s}_2 C(\mathbf{s}_1, \mathbf{s}_2) f_m(\mathbf{s}_2) = \lambda_m f_m(\mathbf{s}_1).$$

Here, $c_m(\theta)$ are a set of uncorrelated random variables (RVs), such that $E[c_m(\theta)] = 0$ and $E[c_m(\theta) c_n(\theta)] = \delta_{n,m} \forall n, m \in \mathbb{N}$. The coefficients $c_m(\theta)$ are related to the RF through projections onto the eigenfunctions, i.e.,

$$(3) \quad c_m(\theta) = \frac{1}{\sqrt{\lambda_m}} \int_{\mathcal{D}} d\mathbf{s} X(\mathbf{s}, \theta) f_m(\mathbf{s}).$$

For a Gaussian RF, $c_m(\theta)$ are independent, normally distributed Gaussian RVs. With a goal to obtain realizations of the random functions that take values in the bounded domain, we will assume that $c_m(\theta)$ are either uniformly distributed or Beta distributions such as B(2,2) and B(2,5) [1]. The presented methodology enables us to employ different types of distributions in different parts of the domain. We can then obtain realizations of the RFs with different covariance functions and correlation lengths.

2.2. Covariance models. Gibbs RFs can effectively express correlations in terms of energy functionals $\mathcal{H}[\cdot]$ measuring the “energy content” of the RF realizations $x(\mathbf{s})$, in the sense that a higher “energy content” implies less probable realizations [9]. The joint probability density function (pdf) of a Gibbs RF is given by

$$(4) \quad f_X[x(\mathbf{s})] = \frac{e^{-\mathcal{H}[x(\mathbf{s})]}}{Z},$$

where the partition function $Z = \int \mathcal{D}x(\mathbf{s}) e^{-\mathcal{H}[x(\mathbf{s})]}$ is the normalizing constant of the pdf and $\int \mathcal{D}x(\mathbf{s})$ denotes the functional integral over all possible realizations. The Spartan spatial random field (SSRF) energy functional \mathcal{H}_{fgc} [9] is defined by

$$(5) \quad \mathcal{H}_{\text{fgc}}[x(\mathbf{s})] = \frac{1}{2\eta_0 \xi^d} \int_{\mathcal{D}} d\mathbf{s} \left\{ [x(\mathbf{s})]^2 + \eta_1 \xi^2 [\nabla x(\mathbf{s})]^2 + \xi^4 [\nabla^2 x(\mathbf{s})]^2 \right\},$$

where the scale coefficient η_0 determines the RF amplitude, the rigidity coefficient η_1 determines the shape of RF realizations (shape parameter), the characteristic length ξ determines, in connection with η_1 , the range of correlations, and d is the dimension of the spatial domain. The SSRF covariance function is permissible for $\eta_1 > -2$ [9]

following Bochner's theorem [2]. The corresponding SSRF is Gaussian, stationary, and isotropic. SSRFs have been generalized to represent nonseparable vector-valued functions [12]. In addition, SSRFs have been extended to the space-time domain [13].

The 1-D SSRF covariance is given in the following form [11, equations (43)–(44), p. 4673]:

$$(6) \quad C(s_1 - s_2) = \begin{cases} \eta_0 \frac{1}{\Delta} \left(\frac{e^{-\frac{|s_1-s_2|}{\xi} \omega_1}}{2\omega_1} - \frac{e^{-\frac{|s_1-s_2|}{\xi} \omega_2}}{2\omega_2} \right), & \eta_1 > 2, \\ \frac{\eta_0}{4} \left(1 + \frac{|s_1-s_2|}{\xi} \right) e^{-\frac{|s_1-s_2|}{\xi}}, & \eta_1 = 2, \\ \eta_0 e^{-\frac{|s_1-s_2|}{\xi}} \beta_2 \left[\frac{\cos(\frac{|s_1-s_2|}{\xi} \beta_1)}{4\beta_2} + \frac{\sin(\frac{|s_1-s_2|}{\xi} \beta_1)}{4\beta_1} \right], & |\eta_1| < 2. \end{cases}$$

In (6) the dimensionless oscillation frequency β_1 and the damping constants $\beta_2, \omega_1, \omega_2$ are functions of the rigidity coefficient η_1 , i.e.,

$$(7) \quad \beta_1 = \frac{|2 - \eta_1|^{\frac{1}{2}}}{2}, \quad \beta_2 = \frac{|2 + \eta_1|^{\frac{1}{2}}}{2},$$

$$(8) \quad \omega_1 = \left(\frac{|\eta_1 - \Delta|}{2} \right)^{\frac{1}{2}}, \quad \omega_2 = \left(\frac{|\eta_1 + \Delta|}{2} \right)^{\frac{1}{2}}, \quad \text{where } \Delta = |\eta_1^2 - 4|^{\frac{1}{2}}.$$

The variance σ^2 of the SSRF model, which is a function of η_1 and η_0 , is obtained from (6) for zero spatial lag when $s_1 = s_2$ and has the following form:

$$(9) \quad \sigma^2 = \begin{cases} \frac{\eta_0}{\Delta} \left(\frac{1}{2\omega_1} - \frac{1}{2\omega_2} \right), & \eta_1 > 2, \\ \frac{\eta_0}{4\beta_2}, & |\eta_1| \leq 2. \end{cases}$$

The correlation length of the SSRF covariance function, which depends on both the shape parameter η_1 and the characteristic length ξ , is given by [22]

$$(10) \quad r_c = \xi \sqrt{|\eta_1|}.$$

For $\eta_1 = 2$, $\eta_0 = 4$, and $\xi = 1/\alpha$, equation (6) recovers the modified exponential covariance model [21]. As we can see in Figure 2, the 1-D SSRF model is differentiable (the proof of SSRF differentiability in one dimension can be found in [11]) and includes oscillating covariances for negative values of the rigidity coefficient η_1 . The negative covariance indicates that the values of the RVs (projections of the RFs onto fixed values of the spatial variable s) can be inversely proportional (namely, one variable can increase while the other decreases). Figure 2 shows different covariance functions obtained by changing η_1 compared in subfigure (d), which plots the covariances as functions of 1-D spatial lag. Other permissible covariance models with oscillatory covariance exist, such as the Matérn (Bessel) covariance functions [18] and the exponentially damped cosine [27].

3. Constructing random nonoverlapping scatterers. The meta-atoms in MMs may have a random variation by design or due to a manufacturing process. Figure 1 shows the sketches of the 2-D and 3-D MMs with randomly located meta-atoms. In this section, we present an approach to produce correlated random scattering objects by perturbing initially uniformly spaced ones. The random locations obtained, however, should satisfy a geometric volume exclusion constraint; namely, no adjacent meta-atoms should overlap. In Figure 3 the distributions of the random positions

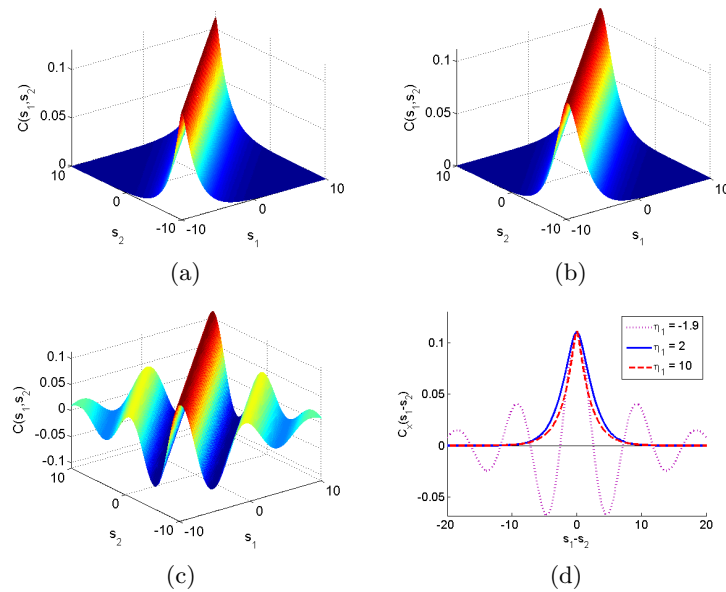


FIG. 2. SSRF covariance functions with variance $\sigma^2 = (1/3)^2$ and correlation length $r_c = 2$. The curves in subfigures (a), (b), (c) are obtained with the following parameter values: scale coefficient $\eta_0 = 0.77, 0.44, 0.07$, rigidity coefficient $\eta_1 = 10, 2, -1.9$, and characteristic length $\xi = 0.63, 1.4, 1.45$. In subfigure (d) we plot the same covariances with respect to the spatial lag.

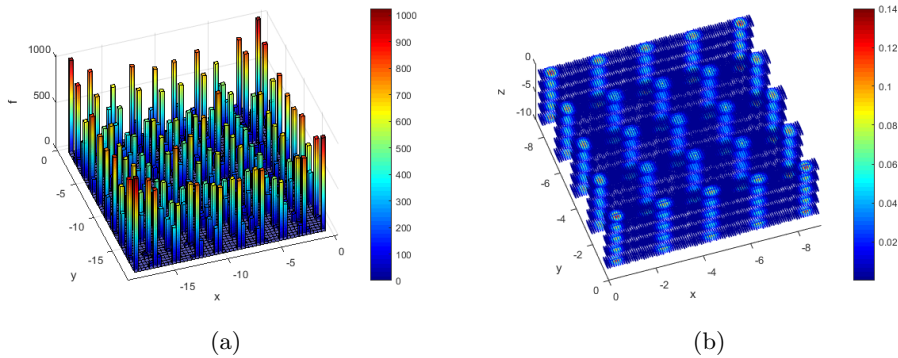


FIG. 3. Distributions of the random positions. Subfigure (a) shows the frequency (f) of the random positions in a 2-D random MM, and subfigure (b) shows the pdf of a 3-D random MM.

acquired by the algorithm that we will present for both a 2-D and a 3-D MM are shown (qualitatively) giving to the configurations in Figure 1. We can observe the so-called entropic clothes-pin effect; i.e., the “pins” or meta-atoms are more likely to cluster near the boundary [16].

Let $\bar{\mathbf{X}}_{\mathbf{n}} = (x_{n_1}, y_{n_2}, z_{n_3})$, with $n_1 = 1, \dots, N_1, n_2 = 1, \dots, N_2, n_3 = 1, \dots, N_3$, and $\mathbf{n} = N_1 \times N_2 \times N_3 = 1, 2, \dots, N$, be the centers of uniformly spaced scattering objects in a 3-D domain $\mathcal{D} = [x_{min} + \frac{l_s}{2}, x_{max} - \frac{l_s}{2}] \times [y_{min} + \frac{l_s}{2}, y_{max} - \frac{l_s}{2}] \times [z_{min} + \frac{l_s}{2}, z_{max} - \frac{l_s}{2}]$, where l_s is the length of an individual scatterer. Let the distance between the centers of scatterers be equal to $\alpha + l_s, b + l_s, c + l_s$ in the x, y, z - directions, respectively, where by α, b, c we denote the distance between the cubes’ edges in

the x -, y -, z -directions, respectively. Our approach is based on first constructing a continuous or refined discrete RF of positions fluctuations with specified correlation and probabilistic distribution functions and then projecting the RF onto a uniform mesh location (the perfect regularly spaced reference meta-atom configuration) to obtain the random scatterers' locations. Thus, an efficient reduction algorithm is used to handle the high dimensionality of the RF, especially in the case of short correlations.

Here we propose the following steps to obtain random correlated scattering objects \mathbf{X}_n :

- *Procedure:* First, we construct continuous RFs of position fluctuations $\Upsilon(\mathbf{s}, \theta) = (v_x(s_1, \theta), v_y(s_2, \theta), v_z(s_3, \theta))$ for $s_1 \in [x_1, x_2]$, $s_2 \in [y_1, y_2]$, $s_3 \in [z_1, z_2]$ with covariance $C_\Upsilon(\mathbf{s} - \mathbf{s}')$. Then, we project them onto a discrete mesh to generate the random distribution of nonoverlapping scatterers \mathbf{X}_n .

1. We assume that the covariance satisfies the separability hypothesis and can be written as a product of 1-D covariances as follows:

$$(11) \quad C_\Upsilon(\mathbf{s} - \mathbf{s}') = C_x(s_1 - s'_1)C_y(s_2 - s'_2)C_z(s_3 - s'_3).$$

We construct the RF $\Upsilon(\mathbf{s}, \theta)$ by an M_i -term ($i = 1, 2, 3$) truncated K-L expansion as in (1) in each direction, $\kappa_i = x, y, z$, as follows:

$$(12) \quad v_{\kappa_i}(s_i, \theta) = \sum_{m_i=1}^{M_i} \sqrt{\lambda_{m_i}} c_{m_i}(\theta) f_{m_i}(s_j),$$

where the unknown random coefficients $c_{m_i}(\theta)$, $i = 1, 2, 3$, are RVs of either uniform or Beta distribution and $\lambda_{m_i}, f_{m_i}(s_i)$ are the eigenvalues and eigenvectors of the covariances of $v_x(s_1, \theta), v_y(s_2, \theta), v_z(s_3, \theta)$, respectively.

In order to have $\Upsilon(\mathbf{s}, \theta) \subseteq [-1, 1]^3$, the variances of the $v_x(s_1, \theta), v_y(s_2, \theta), v_z(s_3, \theta)$ are adjusted to ensure that most of the samples fall inside the bounded domain $[-1, 1]^3$. Clearly, the sum of the uniform RVs in the K-L expansion above will follow a Gaussian distribution closely for a large value of M_i . Therefore, samples of the RF outside $[-1, 1]^3$ will be rejected.

2. We obtain realizations of the continuous RFs $\Upsilon(\mathbf{s}, \theta)$ using ME-PCM sampling for generating the RVs $c_m(\theta)$.
3. Now, the continuous random functions are discretized to obtain RVs on a lattice. To this end, we assume a discrete index ($\mathbf{s} = \mathbf{n}$) and obtain the RVs

$$\Upsilon(\mathbf{n}, \theta) = \Upsilon^n(\theta) = (v_x^{n_1}(\theta), v_y^{n_2}(\theta), v_z^{n_3}(\theta)).$$

4. Finally, we randomize the initially uniformly distributed scatterers $\bar{\mathbf{X}}_n$ using $v_x^{n_1}(\theta), v_y^{n_2}(\theta), v_z^{n_3}(\theta)$ with the following rule:

$$(13) \quad \mathbf{X}_n(\theta) = \bar{\mathbf{X}}_n + \left(\frac{\alpha}{2} v_x^{n_1}(\theta), \frac{b}{2} v_y^{n_2}(\theta), \frac{c}{2} v_z^{n_3}(\theta) \right),$$

where α, b, c is the space between the initial uniformly spaced scatterers along the x -, y -, z - directions, respectively.

- *Implementation of the algorithm:* We assume continuous Spartan RFs with separable covariance $C_\Upsilon(\mathbf{s} - \mathbf{s}')$ defined by (11), where along each dimension we use the model defined by (6). We adjust the scale coefficient η_0 to ensure

that most of the samples fall inside the bounded region $[-1, 1]$. To this end, we consider a target variance σ^2 and then define η_0 using the following formula obtained by (9):

$$(14) \quad \eta_0 = \begin{cases} \frac{\Delta(\omega_2 - \omega_1)}{2\omega_1\omega_2} \sigma^2, & \eta_1 > 2, \\ 4\beta_2 \sigma^2, & |\eta_1| \leq 2, \end{cases}$$

where the parameters ω_1 and ω_2 are given by (8). Similarly, we adjust the characteristic length ξ to obtain a target correlation length r_c by means of (10) for every value of η_1 . We also assume a fixed variance $\sigma^2 = (1/3)^2$. Then, for fixed s , by the Chebyshev inequality, the probability that the RF falls outside $[-1, 1]$ is less than 0.1 and for a Gaussian RF this probability will drop to less than 0.03. In any case, samples outside this region are discarded.

In order to obtain alternative realizations of the MM configuration different from the continuous RFs $\Upsilon(s, \theta)$ above, discrete RVs $\Upsilon(n, \theta)$ can be used in two different approaches. In the first approach (the continuous-discrete approach), we generate and project continuous random paths. In the second approach (the fully discrete approach), we generate random paths on a refined grid. When an analytic solution of the K–L expansion is available, the continuous-discrete approach has computational advantages for high-dimensional lattices and small correlation lengths of the random perturbations because it avoids the spectral decomposition of large covariance matrices. Nevertheless, when the analytic solution of the K–L expansion is not available, the fully discrete approach is a convenient alternative.

1. *The continuous-discrete approach.* When an analytic solution of the K–L expansion exists, we can generate continuous realizations of the random functions $v_x(s_1, \theta)$, $v_y(s_2, \theta)$, $v_z(s_3, \theta)$ given by (12). Explicit formulas for the eigenvalues λ_{m_i} and the eigenvectors $f_{m_i}(s_i)$, $m_i = 1, 2, \dots, M_i$, of the K–L expansion of the 1-D SSRF covariance model are available in [22]. These were obtained by the solution of the homogeneous Fredholm integral equation of the second kind (2). For the SSRF covariance kernel the integral equation (2) leads to a fourth-order linear ordinary differential equation (KL-ODE). More precisely, for $\eta_1 \geq 0$ the eigenvalues are given as the solutions of two transcendental equations available in [22, equations (23) and (25)] and the corresponding eigenvectors in [22, equations (29) and (30)]. For damped oscillating covariances ($\eta_1 < 0$) two families of eigenvalues/eigenfunctions must be considered corresponding to the two branches of the KL-ODE. These two families of eigenvalues are the solutions of the transcendental equations in [22, equations (23), (25), (26), and (28)] and of the eigenvectors given in [22, equations (29), (30), (35), and (36)]. The sampling points $c_{m_i}(\theta)$, $m_i = 1, 2, \dots, M_i$, are RVs of either uniform or Beta distribution. Thus, the random dimension of the problem is equal to $M_1 + M_2 + M_3$. The multi-element probabilistic collocation method (ME-PCM) [7] will be used to compute moments of RVs where the sampling points for the RVs are Gauss quadrature points based on different types of orthogonal polynomials $P_n(x)$; for uniformly distributed RVs we consider Legendre polynomials, whereas for Beta distributed RVs we consider Jacobi polynomials [26]. Here, for uniform RVs, we obtain the collocation points in each stochastic dimension, and then we obtain the high dimension collocation points based on a tensor product rule. We use the freely available software MEPCMP (V1.01) [28, 25, 7, 29].

In Figure 4, five different realizations obtained by the truncated K–L expansion of a 1-D RF $v_x(s_1, \theta)$ are depicted. In each subfigure, filled markers depict the RVs $v_x^{n_1}(\theta)$, for $n_1 = 1, 2, \dots, 20$, which are the projections of the RFs onto a regularly

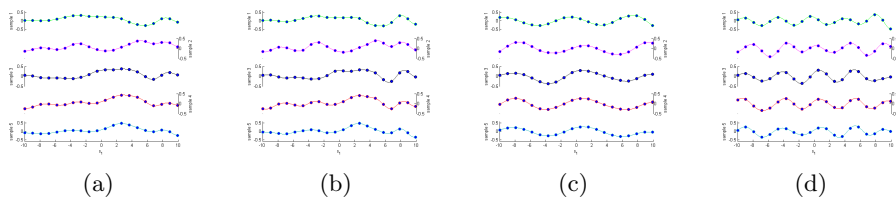


FIG. 4. Realizations of 1-D continuous random functions of position fluctuations $v_x(s_1, \theta)$ (solid lines). In each realization solid circles depict the projections onto a regularly spaced configuration mesh of 19 meta-atoms. In each subfigure, five different realizations of the same random function are plotted. In subfigure (a) $\eta_1 = 2$, $r_c = 2$, in (b) $\eta_1 = 2$, $r_c = 1$, in (c) $\eta_1 = -1.99$, $r_c = 2$, in (d) $\eta_1 = -1.99$, $r_c = 1$.

TABLE 1

Relative approximated energy of the truncated K-L expansion of an SSRF model with variance $\sigma^2 = (1/3)^2$ for different combinations of correlation length r_c , shape parameter η_1 , and the number of K-L terms.

Relative approximated energy (%)						
# of K-L terms	5		10		15	
r_c	1	2	1	2	1	2
$\eta_1 = 5$	49.05	72.99	73.86	90.76	85.34	96.02
$\eta_1 = 2$	57.98	82.92	83.95	96.39	93.16	98.82
$\eta_1 = -1.99$	87.17	94.75	95.69	99.65	99.03	99.92

spaced configuration mesh. The five different subplots correspond to different configurations of the SSRF model. As the rigidity coefficient approaches the permissibility boundary, for $\eta_1 = -1.99$ in subfigures (c) and (d), the sample functions of the SSRF model exhibit an almost regular oscillatory behavior.

The mean energy E_{tot}^D of an RF $v_x(s_1, \theta)$ for $s_1 \in \mathcal{D} = [x_{min}, x_{max}]$ can be defined in terms of the RF variance

$$(15) \quad E_{tot}^D = E^\theta \left[\int_{x_{min}}^{x_{max}} ds_1 (v_x(s_1, \theta))^2 \right] = |x_{max} - x_{min}| \cdot \sigma_{u_x}^2.$$

Replacing the M_1 -term truncated K-L expansion given by (12) of $v_x(s_1, \theta)$ in the integral equation (15), invoking the orthogonality of the eigenfunctions and the independence of the random parameters we obtain the following equation for the approximated cumulative mean energy $E_{M_1}^D$:

$$(16) \quad E_{tot}^D = |x_{max} - x_{min}| \cdot \sigma_{u_x}^2 \approx E_{M_1}^D = \sum_{m_1}^{M_1} \lambda_{m_1}.$$

We list the relative approximated energy $E_{M_1}^{rel} = E_{M_1}^D / E_{tot}^D$ in Table 1 for an SSRF covariance with variance $\sigma^2 = (1/3)^2$, different correlation lengths, rigidity coefficients η_1 , and the number of K-L terms. As we can see, the K-L series converges more slowly as the correlation length becomes shorter. The dimensionality problem becomes more severe for even shorter correlation lengths. For example, for $r_c = 0.1$ we need more than 122 K-L terms to reach 90% of the relative approximated energy for $\eta_1 = 2$, more than 102 for $\eta_1 = -1.9$, and more than 88 for $\eta_1 = -1$. A discussion about faster convergence of the K-L series for the same correlation length r_c and different values of rigidity coefficient η_1 , as well as more details regarding the convergence of the SSRF K-L series, can be found in [22].

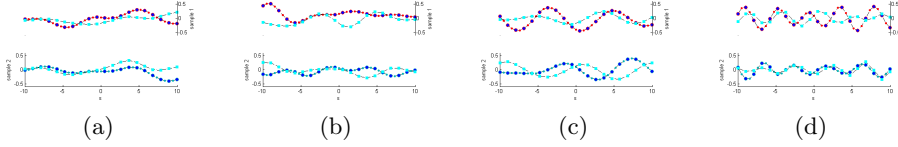


FIG. 5. Realizations of 1-D discrete RFs of position fluctuations $v_x^{\tilde{n}_1}(\theta)$ on a refined grid for $r_1 = 2$ (round markers) and directly obtained on the regularly spaced configuration grid for $r_1 = 1$ (square markers). In the realization obtained on a refined grid, the larger round markers depict the projections onto a regularly spaced configuration mesh of 19 meta-atoms. In each subfigure, two different realizations of the same random function are plotted; SSRFs in subfigures (a)–(d) have the same parameters as in Figure 4.

2. *The fully discrete approach.* Alternatively, we can adopt a fully discrete approach. Let $\mathbf{X}_{\tilde{\mathbf{n}}} = (\tilde{x}_{\tilde{n}_1}, \tilde{y}_{\tilde{n}_2}, \tilde{z}_{\tilde{n}_3})$, with $\tilde{n}_i = 1, \dots, \tilde{N}_i$, where $\tilde{n}_i = r_i n_i$, $r_i \in \mathbb{N}$ is a positive integer, and $i = 1, 2, 3$, be a refinement of the regularly spaced reference meta-atom configuration mesh. The discrete RVs

$$\Upsilon(\tilde{\mathbf{n}}, \theta) = \Upsilon^{\tilde{\mathbf{n}}}(\theta) = (v_x^{\tilde{n}_1}(\theta), v_y^{\tilde{n}_2}(\theta), v_z^{\tilde{n}_3}(\theta))$$

are the projections of the centered RF $\Upsilon(\mathbf{s}, \theta)$ onto a fine mesh (compared with the uniformly spaced meta-atoms) when we assume the discrete index $\mathbf{s} = \tilde{\mathbf{n}}$. These projections consist of the discrete parameter L^2 processes $\Upsilon_x^{\tilde{n}_1}(\theta) = \{v_x^{\tilde{n}_1}\}_{\tilde{n}_1=1,2,\dots,\tilde{N}_1}$, $\Upsilon_y^{\tilde{n}_2}(\theta) = \{v_y^{\tilde{n}_2}\}_{\tilde{n}_2=1,2,\dots,\tilde{N}_2}$, and $\Upsilon_z^{\tilde{n}_3}(\theta) = \{v_z^{\tilde{n}_3}\}_{\tilde{n}_3=1,2,\dots,\tilde{N}_3}$ along the x -, y -, z -directions, respectively. Since we have assumed that $C_\Upsilon(\mathbf{s} - \mathbf{s}')$ follows the separability hypothesis along the direction coordinates, the same will be true for the discrete projections $\Upsilon_x^{\tilde{n}_1}(\theta), \Upsilon_y^{\tilde{n}_2}(\theta), \Upsilon_z^{\tilde{n}_3}(\theta)$. Hence, using the analytic formulas for the covariances in each direction we obtain the real symmetric covariance matrices of the RFs on the discrete locations n_i , $i = 1, 2, 3$; for example, the covariance matrix along the x -coordinate direction will be given by

$$(17) \quad (\Sigma^{\Upsilon_x^{\tilde{n}_1}})_{\mu_1, \nu_1=1,2,\dots,\tilde{N}_1} = \mathbb{E}^\theta[(v_x^{\mu_1}(\theta)v_x^{\nu_1}(\theta))]_{\mu_1, \nu_1} = (C_x(\tilde{x}_{\mu_1} - \tilde{x}_{\nu_1}))_{\mu_1, \nu_1}.$$

According to the spectral representation theorem for real symmetric matrices, if $(\tilde{f}_{\tilde{n}_i}(\tilde{x}_{\tilde{n}_i}))_{\tilde{n}_i=1,2,\dots,\tilde{N}_i}$ and $\lambda_{\tilde{m}_i}$, for $i = 1, 2, 3$, are the eigenvectors and eigenvalues of the covariance matrices $(\Sigma^{\Upsilon_x^{\tilde{n}_1}})_{\mu_1, \nu_1}, (\Sigma^{\Upsilon_y^{\tilde{n}_2}})_{\mu_2, \nu_2}, (\Sigma^{\Upsilon_z^{\tilde{n}_3}})_{\mu_3, \nu_3}$, respectively, the discrete random functions $\Upsilon^{\tilde{\mathbf{n}}}(\theta)$ can be expanded by an \tilde{M}_i -term ($i = 1, 2, 3$) truncated series in each direction that in the x -coordinate direction, for example, will read as follows:

$$(18) \quad \Upsilon_x^{\tilde{n}_1}(\theta) = (v_x^{\tilde{n}_1})_{\tilde{n}_1} = \sum_{\tilde{m}_1=1}^{\tilde{M}_1} \sqrt{\lambda_{\tilde{m}_1}} c_{\tilde{m}_1}(\theta) (\tilde{f}_{\tilde{m}_1}(\tilde{x}_{\tilde{n}_1}))_{\tilde{n}_1}.$$

In (18), the unknown random coefficients $c_{\tilde{m}_1}(\theta)$ are RVs of either uniform or Beta distribution. Then, it is straightforward to obtain the projection of the RVs $\Upsilon^{\tilde{\mathbf{n}}}(\theta)$ from a fine mesh to the regularly spaced reference meta-atom mesh.

In Figure 5, two different realizations obtained by the fully discrete approach are depicted. In each subfigure, square markers depict discrete RFs of position fluctuations $v_x^{\tilde{n}_1}(\theta)$ directly obtained on the regularly spaced configuration grid for $r_1 = 1$. Round markers depict $v_x^{\tilde{n}_1}(\theta)$ obtained on a refined grid for $r_1 = 2$ with the larger round markers depicting the projections onto the reference meta-atom configuration

TABLE 2

Relative approximated energy of the truncated K–L expansion of a projected SSRF model onto a discrete mesh that is a refinement of the regularly spaced reference meta-atom configuration mesh. The variance is $\sigma^2 = (1/3)^2$, the shape parameter is $\eta_1 = 2$, and different combinations of correlation length r_c , the size of the reference meta-atom configuration mesh N_1 , and the number of K–L terms are considered.

Relative approximated energy / Mesh refinement $r = 2$						
# of K–L terms	5		10		15	
r_c	1	2	1	2	1	2
$N_1 = 10$	56.51	81.62	83.75	96.19	<i>94.56</i>	<i>99.01</i>
$N_1 = 15$	56.78	82.02	83.27	96.16	93.07	98.75
$N_1 = 20$	57.04	82.23	83.34	96.19	92.92	98.76
$N_1 = 30$	57.34	82.46	83.51	96.25	92.94	98.77

TABLE 3

The same as in Table 2 when the continuous RFs are directly projected onto the regularly spaced reference meta-atom configuration mesh.

Relative approximated energy / No refinement						
# of K–L terms	5		10		15	
r_c	1	2	1	2	1	2
$N_1 = 5$	<i>100</i>	<i>100</i>	–	–	–	–
$N_1 = 10$	<i>60.76</i>	<i>81.53</i>	<i>100</i>	<i>100</i>	–	–
$N_1 = 15$	56.85	81.35	<i>85.88</i>	<i>96.53</i>	<i>100</i>	<i>100</i>
$N_1 = 20$	56.51	81.62	83.75	96.19	<i>94.56</i>	<i>99.01</i>
$N_1 = 30$	56.78	82.02	83.27	96.16	93.07	98.79

mesh. The five different subplots correspond to different configurations of the SSRF model.

Let the mean energy of the RF $\{\Upsilon_x^{\tilde{n}_1}\}_{\tilde{n}_1=1,\dots,\tilde{N}_1}$ be defined by the equation

$$(19) \quad \tilde{E}_{tot}^{\tilde{N}_1} = \mathbb{E}^\Theta [\Upsilon_x^{\tilde{n}_1}(\theta)]^2 = \tilde{N}_1 \cdot \sigma_{u_x}^2,$$

which is the discrete analogue of (15). Replacing the approximation given by (18) in (19) we obtain the discrete analogue of (16):

$$(20) \quad \tilde{E}_{tot}^{\tilde{N}_1} = \tilde{N}_1 \cdot \sigma_{u_x}^2 \approx E_{\tilde{M}_1}^{\tilde{N}_1} = \sum_{\tilde{m}_1}^{\tilde{M}_1} \lambda_{\tilde{m}_1}.$$

In Tables 2 and 3 we list the relative approximated energy $\tilde{E}_{\tilde{M}_1}^{rel} = \tilde{E}_{\tilde{M}_1}^{\tilde{N}_1} / \tilde{E}_{tot}^{\tilde{N}_1}$ for an SSRF covariance with variance $\sigma^2 = (1/3)^2$, rigidity coefficient $\eta_1 = 2$, different correlation lengths, the number of K–L terms, and the size of the regularly spaced reference meta-atom configuration mesh N_1 . In Table 2 we consider a refinement $r_1 = 2$ of the reference meta-atom configuration mesh, whereas in Table 3 (for $r_1 = 1$) the continuous RFs are directly projected onto the reference meta-atom configuration mesh. Comparing Tables 2, 3, and 1, for $\eta_1 = 2$, we observe that in most cases the continuous approach results in a faster convergence of the K–L series followed by the case where a refinement is considered. The cases where the discrete approach leads to a faster convergence of the K–L series correspond to the sparser configuration meshes and are emphasized in italics in Tables 2 and 3. For the sparser configurations the relative approximated energy reaches 100% when the number of K–L terms allows for a full spectral decomposition of the covariance matrix. This discrepancy indicates that for a sparse mesh the model is not sensitive to all the variability of the RFs.

4. Electromagnetic waves in random layered media. In this section, we apply the proposed methodology to generate a random layered heterojunction and compute its transmission properties with a transmission or scattering matrix formulation. Sommerfeld outgoing radiation conditions [3] are implied for the scattering part (above the topmost layer) and transmitting wave (below the bottommost layer).

4.1. The transfer matrix method. We consider a horizontally y -polarized transverse magnetic (TM) wave $\mathbf{H} = (0, H_y, 0)$ in a random n -layer heterojunction with a normal direction along the z -coordinate direction with different dielectric constants ϵ_i (permittivity) and μ_i (permeability) associated with each layer of width D_i . After a Fourier transform in the horizontal x - and y -directions, the y -component of the transverse magnetic (TM) wave $\psi_i(z) = H_y(z)$ in the i th layer for each realization of the random layers satisfies the 1-D Helmholtz equation

$$(21) \quad \frac{\partial^2 \psi_i(z)}{\partial z^2} + (k_i^2 - k_\rho^2) \psi_i(z) = 0,$$

where $k_\rho^2 = k_x^2 + k_y^2$ is the wave number of the incoming wave, and the wave number in the i th layer is given by $k_i^2 = \omega^2 \epsilon_i \mu_i$. The solution to (21) in each layer is given by (more details can be found in [5])

$$(22) \quad \psi_i = a_i e^{u_i z_i} + b_i e^{-u_i z_i},$$

where $u_i = \sqrt{k_\rho^2 - k_i^2}$, and $z_i = z - D_i$.

The value and the slope of the wave function are continuous across the interfaces between layers. Matching at the interface $z_{i+1} = D_{i+1}$ or $z_i = 0$ gives

$$(23) \quad a_i e^{u_i 0} + b_i e^{-u_i 0} = a_{i+1} e^{u_{i+1} D_{i+1}} + b_{i+1} e^{-u_{i+1} D_{i+1}},$$

$$(24) \quad a_i u_i e^{u_i 0} - b_i u_i e^{-u_i 0} = a_{i+1} u_{i+1} e^{u_{i+1} D_{i+1}} - b_{i+1} u_{i+1} e^{-u_{i+1} D_{i+1}}.$$

By solving for a_i and b_i in terms of a_{i+1} and b_{i+1} the transfer matrix $T(i + 1)$ between the i th and $(i + 1)$ th layers can be found as

$$(25) \quad \begin{bmatrix} a_i \\ b_i \end{bmatrix} = T(i + 1) \begin{bmatrix} a_{i+1} \\ b_{i+1} \end{bmatrix},$$

where

$$(26) \quad T(i + 1) = \frac{1}{2} \begin{bmatrix} (1 + \frac{u_{i+1}}{u_i}) \exp(u_{i+1} D_{i+1}) & (1 - \frac{u_{i+1}}{u_i}) \exp(-u_{i+1} D_{i+1}) \\ (1 - \frac{u_{i+1}}{u_i}) \exp(u_{i+1} D_{i+1}) & (1 + \frac{u_{i+1}}{u_i}) \exp(-u_{i+1} D_{i+1}) \end{bmatrix} \\ = \begin{bmatrix} T_{11}(i + 1) & T_{12}(i + 1) \\ T_{21}(i + 1) & T_{22}(i + 1) \end{bmatrix}.$$

The inverse of a transfer matrix is also a transfer matrix $I(i + 1) = T^{-1}(i + 1)$:

$$(27) \quad \begin{bmatrix} a_{i+1} \\ b_{i+1} \end{bmatrix} = I(i + 1) \begin{bmatrix} a_i \\ b_i \end{bmatrix},$$

where

$$(28) \quad I(i + 1) = \frac{1}{2} \begin{bmatrix} (1 + \frac{u_i}{u_{i+1}}) \exp(-u_{i+1} D_{i+1}) & (1 - \frac{u_i}{u_{i+1}}) \exp(-u_{i+1} D_{i+1}) \\ (1 - \frac{u_i}{u_{i+1}}) \exp(u_{i+1} D_{i+1}) & (1 + \frac{u_i}{u_{i+1}}) \exp(u_{i+1} D_{i+1}) \end{bmatrix}.$$

Equation (26) can be generalized so that we can compute the transmission and reflection coefficients for wave propagation through the n -layer. In fact, the equivalent transfer matrix expression will be given by

$$(29) \quad \mathbf{I}(n) = \mathbf{T}^{-1}(n) \mathbf{T}^{-1}(n-1) \dots \mathbf{T}^{-1}(2) \mathbf{T}^{-1}(1).$$

The transmission and reflection amplitudes $t(n), r(n)$ to the n -layer can be computed from the elements of the matrix $\mathbf{I}(n)$:

$$(30) \quad t(n) = \frac{1}{I_{22}(n)}, \quad r(n) = \frac{-I_{21}(n)}{I_{22}(n)}.$$

4.2. Scattering matrix method. For a system with a large number of layers, the transfer matrix method can become unstable due to the exponentially growing waves, resulting in information lost in the calculations. An equivalent scattering matrix formulation, which couples the incoming with the outgoing waves, allows the separation of the exponentially growing terms from the exponentially decaying terms, resulting in a more stable calculation [15].

Let $\mathbf{S}(1)$ be the scattering matrix between layers 0 and 1, namely

$$(31) \quad \begin{bmatrix} a_1 \\ b_0 \end{bmatrix} = \mathbf{S}(1) \begin{bmatrix} a_0 \\ b_1 \end{bmatrix},$$

$$(32) \quad \mathbf{S}(1) = \Lambda \begin{bmatrix} 2u_0 & -(u_0 - u_1)e^{-u_1 D_1} \\ (u_0 - u_1)e^{u_1 D_1} & 2u_1 \end{bmatrix} = \begin{bmatrix} S_{11}(1) & S_{12}(1) \\ S_{21}(1) & S_{22}(1) \end{bmatrix},$$

and $\Lambda = \frac{1}{(u_0 + u_1)e^{u_1 D_1}}$.

The scattering matrix for the propagation to the n -layer can be written as

$$(33) \quad \begin{bmatrix} a_n \\ b_0 \end{bmatrix} = \mathbf{S}(n) \begin{bmatrix} a_0 \\ b_n \end{bmatrix} = \begin{bmatrix} S_{11}(n) & S_{12}(n) \\ S_{21}(n) & S_{22}(n) \end{bmatrix} \begin{bmatrix} a_0 \\ b_n \end{bmatrix},$$

where

$$(34) \quad S_{11}(n) = [T_{11}(n) - S_{12}(n-1)T_{21}(n)]^{-1}S_{11}(n-1),$$

$$(35) \quad S_{12}(n) = [T_{11}(n) - S_{12}(n-1)T_{21}(n)]^{-1}[S_{12}(n-1)T_{22}(n) - T_{12}(n)],$$

$$(36) \quad S_{21}(n) = [S_{22}(n-1)T_{21}(n)S_{11}(n) + S_{21}(n-1)],$$

$$(37) \quad S_{22}(n) = [S_{22}(n-1)T_{21}(n)S_{12}(n) + S_{22}(n-1)T_{22}(n)].$$

The transmission and reflection amplitudes $t(n), r(n)$ can be computed from $\mathbf{S}(n)$:

$$(38) \quad t(n) = S(n)_{21}, \quad r(n) = S(n)_{11}.$$

4.3. Transmission and reflection coefficients.

4.3.1. Uniform case. The transmission and reflection coefficients T^n, R^n of the n -layer heterojunction under an incoming wave can be evaluated by the transmission and reflection amplitudes $t(n), r(n)$ using either the transfer or the scattering matrix method. In fact, given the amplitudes of the reflection and transmission coefficients, T^n and R^n can be computed simply by

$$(39) \quad T^n = |t(n)|^2, \quad R^n = |r(n)|^2.$$

Here we assume a uniform structure. All layers have constant width $D_i = D = 1$ and $k_1, k_3, \dots, k_{2N-1} = 1$, while $k_2, k_4, \dots, k_{2N-2} = 1.8$. The transmission and reflection coefficients for 19 and 39 layers have been computed by both methods with a high degree of agreement. The layers are initially uniformly distributed in $[(-2N + 1) D, 0]$ as the computational domain.

4.3.2. Random case. Next, we consider a $(2N - 1)$ -layer heterojunction, having N -layers of constant thickness $D_{n_3} = D$ interchanging with $N - 1$ layers of thickness $D'_{n_2} = D'$, initially equal to D , and the heterojunction is separated by $2N$ interfaces z_n . We assume that the $2N - 1$ layers are uniformly distributed in the initial computational domain $[(-2N + 1) D, 0]$. Using the algorithm presented in the previous section we randomize the thicknesses D'_{n_2} using correlated random variables $v_z^{n_3}(\theta), n_3 = 1, 2, \dots, N$, with a target probabilistic structure such that the layers do not overlap. More precisely, if we denote the centers of the layers of constant thickness D by $\bar{z}_{n_3}, n_3 = 1, 2, \dots, N$, we randomize the constant thickness layer centers using the 1-D version of (13):

$$(40) \quad z_{n_3}(\theta) = \bar{z}_{n_3} + \frac{D'}{2} v_z^{n_3}(\theta), \quad n_3 = 1, 2, \dots, N.$$

In this case, the layers of constant thickness D are indeed nonoverlapping as

$$(41) \quad z_{n_3+1}(\theta) - z_{n_3}(\theta) = D + D' + \frac{D'}{2} (v_z^{n_3+1}(\theta) - v_z^{n_3}(\theta));$$

with $\min\{v_z^{n_3+1}(\theta), \theta \in \Theta\} = -1, \max\{v_z^{n_3+1}(\theta), \theta \in \Theta\} = 1$, we can see that $z_{n_3+1}(\theta) - z_{n_3}(\theta) \geq D$. The computational domain of the random problem is $[(-2N + 1) D - D', D']$.

The set $\{z(\theta), n = 1, 2, \dots, 2N\} = \{z_1(\theta) \mp \frac{D}{2}, z_2(\theta) \mp \frac{D}{2}, \dots, z_{2N}(\theta) \mp \frac{D}{2}\}$ provides the edges of the random heterojunction whose random transmission and reflection coefficients to the n -layer $T^n(\theta), R^n(\theta)$ are given by (29) and (33), which will now depend on the correlated random variables $\{v_z^{n_3}(\theta)\}_{n_3=1,2,\dots,N}$.

We set up the case where the total thickness of the random heterojunction is fixed to the size of the initial computational domain. In order to achieve this the centers of the first and the last layers are kept unperturbed, i.e., $v_z^1(\theta) = v_z^N(\theta) = 0$. In this case, we also observe the so-called entropic force “clothes-pin” effect; i.e., the “pins,” the random layers in our case, are more likely to be closer to the boundary as if they were attracted to it and also more likely to be closer to each other [16]. The latter results in a kind of oscillatory distribution of the positions of the layers.

5. Correlation effects of random MMs on reflection and transmission.

In this section, we will study the effects of correlated randomness in the distance between the layers of a heterojunction onto its transmission and reflection coefficients.

We obtain the first- and second-order moments as well as the maximum and minimum values of the transmission and reflection coefficients for different values of the correlation length r_c and of the shape parameter η_1 of the SSRF model given by (6). We study the above cases of randomness in connection with the geometric constraint of constant total thickness of the heterojunction.

5.1. Moments of transmission and reflection coefficients. The moments of the transmission and reflection coefficients of the random heterojunctions are computed by generating samples of the RFs of position fluctuations $v_z(s, \theta)$ using the M -term truncated K–L expansion

$$(42) \quad v_z(s, \theta) = \sum_{m=1}^M \sqrt{\lambda_m} c_m(\theta) f_m(s),$$

which are then discretized to obtain the random perturbations of the perfect regularly spaced reference layer configuration. Each of the random parameters $c_m(\theta)$, $m = 1, 2, \dots, M$, is sampled at Q collocation nodes $c_m^{(q)}$ with corresponding weights $w_m^{(q)}$, $q = 1, \dots, Q$, where $c_m^{(q)}$ are q -order roots of Legendre polynomials $P_Q(x)$ [25] and

$$(43) \quad w_m^{(q)} = \frac{1 - (c_m^{(q)})^2}{(Q+1)^2 P_{Q+1}(c_m^{(q)})^2}.$$

The total number of collocation nodes and weights for the M -dimensional random space is obtained by a tensor product rule using MEPCMP(V1.01) [28]. Thus, for Q collocation points in each random dimension the total number of collocation points is equal to Q^M (this cost can be significantly reduced by using sparse grids (SGs) of low level in the ME-PCM). The continuous samples are then projected to obtain the RV $v_z^{n_3}(\theta)$, $n_3 = 1, 2, \dots, N$, for a $(2N-1)$ th-layer heterojunction. The p -order moments of transmission and reflection coefficients $T^{2N-1}(\theta) = f(c_1(\theta), \dots, c_M(\theta))$ correspond to the weighted sum of the samples

$$(44) \quad \mathbb{E}^\theta [T^{2N-1}(\theta)^p] = \sum_{q=1}^Q \cdots \sum_{q=1}^Q f^p(c_1^{(q)}, \dots, c_M^{(q)}) \cdot \omega_1^{(q)} \cdots \omega_M^{(q)}.$$

The mean value and the variance of the transmission and reflection coefficients are sensitive to the correlation length, the shape parameter, and the geometric constraint of total thickness. Next, we will present results for the transmission coefficient. The corresponding analysis for the reflection coefficient can be easily induced by the relation $T^{2N-1} + R^{2N-1} = 1$. This defining property of the two coefficients is also verified by our separate calculations for T^{2N-1} and R^{2N-1} using the transfer or scattering matrix method.

Dependence on correlation length. In Figure 6 we plot the mean value and the standard deviation of the transmission coefficient of a random 19-layer heterojunction against the wave number of the incoming wave k_ρ . The centers of the layers of constant thickness were obtained by (40) for $v_z^{n_3}(\theta)$, $n_3 = 1, 2, \dots, 10$. The correlation length r_c varies from 1 to 10 with step 1 for $\eta_1 = 2$. The moments were obtained by applying (44) for $M = 10$ random dimensions for all correlation lengths except for $r_c = 1$, where we used $M = 15$ and two collocation points in each dimension, imposing the additional geometrical constraint of constant total thickness. We can observe

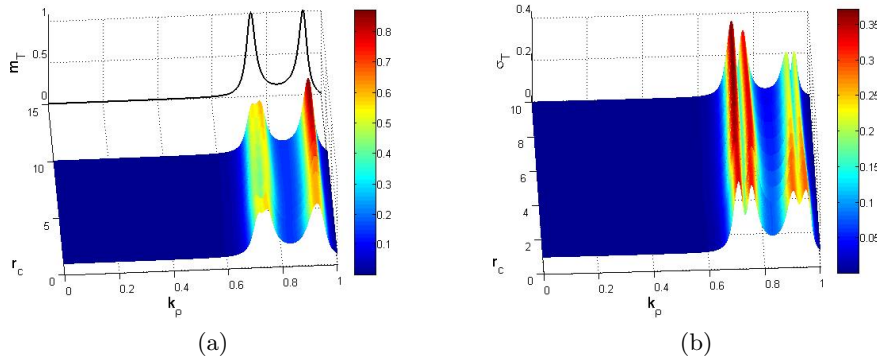


FIG. 6. A 19-layer heterojunction with a constant total thickness: (a) 3-D plot of the mean value (m_T) of the transmission coefficient for different values of the correlation length and the wave number. The transmission coefficient for the reference periodic case is plotted with a solid black line. (b) 3-D plot of the standard deviation (σ_T) of the transmission coefficient. In the plots, we use the SSRF model with $\eta_1 = 2$ for different correlation lengths.

that for all the values k_ρ of the incoming wave, the mean value of the transmission coefficient increases with the correlation length. Additionally, for almost all the values of k_ρ the mean values of the transmission coefficient of the random heterojunctions are smaller than the transmission coefficient of the uniformly spaced heterojunction that is plotted in subfigure (a) with a solid black line. On the contrary, the standard deviation decreases with the correlation length. The large variances of the transmission for short range correlated layers indicate that these cases can be used to obtain heterojunctions with optimized properties. The presence of the geometric constraint of constant thickness slightly affects the moments of the transmission coefficient leading to a difference that reaches 10% for different correlation lengths varying from 1 to 5 and different values of the wave number of the incoming wave.

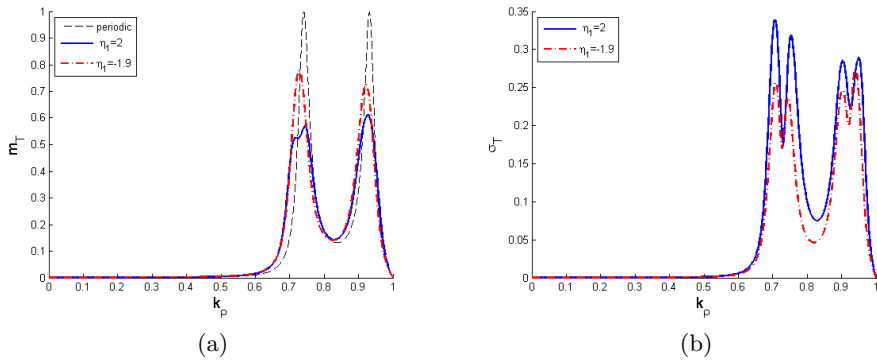


FIG. 7. (a) Mean value of the transmission coefficient of a 19-layer heterojunction for different values to the shape parameter η_1 . The transmission coefficient for the reference periodic case is plotted with a dashed line. (b) The standard deviation of the transmission coefficient. In the plots we use the SSRF model with correlation length $r_c = 1$.

In Figure 7 the mean value and the standard deviation of the transmission coefficient are plotted with respect to the wave number of the incoming wave for different values of the shape parameter of the covariance functions $\eta_1 = 2$ and $\eta_1 = -1.9$.

We can observe that for constant correlation length, here $r_c = 1$, the shape of the covariance also affects the transmission coefficient. For $\eta_1 = -1.9$ the transmission coefficient has larger mean value and smaller standard deviation than the case of $\eta_1 = 2$. It is noted that the mean value and the standard deviation of the transmission coefficient are maximized for different values of k_ρ for $\eta_1 = -1.9$ and $\eta_1 = 2$.

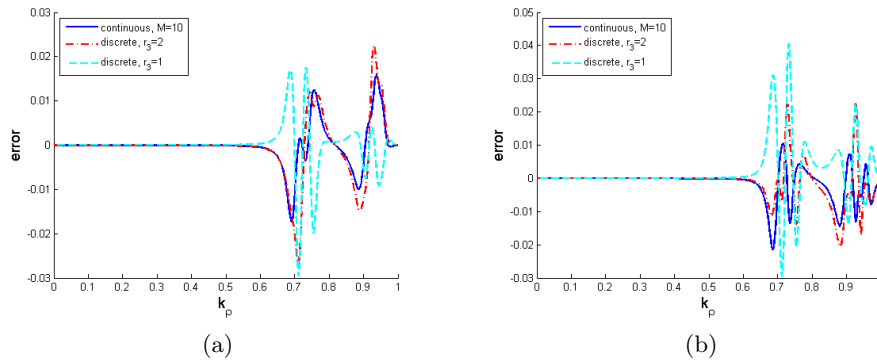


FIG. 8. (a) Differences between the mean value of the transmission coefficient of a 19-layer heterojunction for $\eta_1 = 2$ and $r_c = 1$ (case plotted also in Figures 6 and 7) and when we (i) follow the continuous approach but consider $M = 10$ random dimensions instead of $M = 15$, (ii) follow the fully discrete approach with a refinement $r_3 = 2$, and (iii) follow the discrete approach with no refinement. In cases (ii) and (iii) we also consider $M = 10$ random dimensions. (b) The same as in (a) for the standard deviation of the transmission coefficient.

In Figure 8 we plot the differences between the mean value (a) and the standard deviation (b) of the transmission coefficient for $r_c = 1$ and $\eta_1 = 2$, where the mean value and the standard deviation are obtained using other parameters and implementations of the method. More precisely, we plot the differences between reference moments, obtained with $M = 15$ random dimensions and the continuous-discrete approach, with the moments obtained with $M = 10$ random dimensions and three other implementations of the methodology. The three implementations are (i) the continuous-discrete approach, (ii) the fully discrete approach with a refinement (for $r_3 = 2$), and (iii) the fully discrete approach with no refinement (for $r_3 = 1$). We can observe that errors decrease with the refinement and that, in general, the implementations are in pretty good agreement, with the peaks of the mean value error corresponding to less than 6% in all cases, although the number of samples drops drastically to 1024 from 32768 samples. In the following subsection, we will explore the realizations that maximize or minimize the transmission and reflection coefficients.

5.2. Random heterojunctions that maximize and minimize the transmission coefficients. Let T_{max} and T_{min} be the transmission coefficients of some optimized heterojunctions corresponding to the realizations $\theta_{max}, \theta_{min}$ defined by

$$(45) \quad T_{max}(\eta_1, r_c) = T_{max}(\theta_{max}, \eta_1, r_c),$$

where θ_{max} is defined by the equation

$$(46) \quad IT_{max}(\theta_{max}, \eta_1, r_c) = \max_{\theta \in \Theta} \int_0^1 T(\theta, \eta_1, r_c, k_\rho) dk_\rho,$$

and similarly

$$(47) \quad T_{min}(\eta_1, r_c) = T_{min}(\theta_{min}, \eta_1, r_c),$$

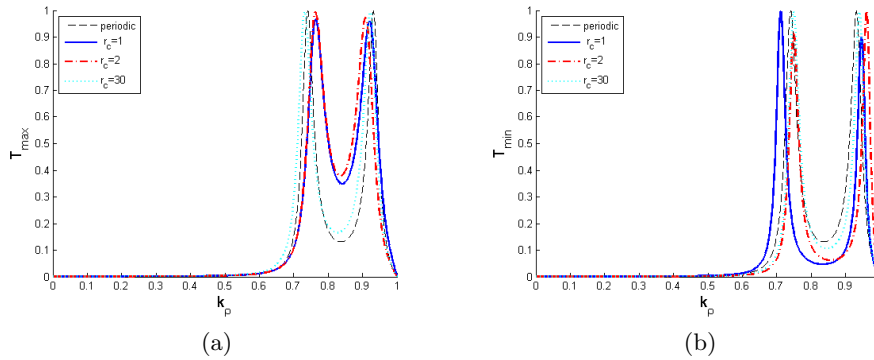


FIG. 9. (a) Maximum transmission coefficients (T_{max}) for a 19-layer heterojunction for different correlation lengths r_c and wave numbers k_p . (b) Minimum values of the transmission coefficient (T_{min}).

where θ_{min} is defined by the equation

$$(48) \quad IT_{min}(\theta_{min}, \eta_1, r_c) = \min_{\theta \in \Theta} \int_0^1 T(\theta, \eta_1, r_c, k_p) dk_p.$$

In Figure 9 we plot the transmission coefficients T_{max} (subfigure (a)) and T_{min} (subfigure (b)) versus the wave number of the incoming wave and different values of the correlation length for $\eta_1 = 2$. These results were obtained using 1024 collocation points for a 19-layer heterojunction of constant thickness and for three different values of the correlation length, i.e., $r_c = 1, 2, 30$, and we also plot the reference uniform case. The random samples were generated using the fully discrete approach with a refinement $r_3 = 2$. From these results, we can see that random short range correlated heterojunctions can have increased transmission coefficients compared to the uniform case for a broader range of the values of the energy of the incoming wave. For large correlation lengths the transmission coefficients approach the values of the uniform reference case, as expected.

In Figure 10 we plot the distances between the centers of the layers of constant thickness $z_{n_3}(\theta)$, $n_3 = 1, 2, \dots, N$, defined by (41), corresponding to the heterojunction with maximum and minimum transmission coefficients. The random distances plotted in subfigure (a) are the ones that maximize the transmission coefficient, whereas the random distances plotted in subfigure (b) are the ones that minimize the transmission coefficient. Results are presented for the same values of the correlation length as in Figure 9. As we can see, the heterojunctions that maximize the transmission coefficient (in subfigure (a)) follow a similar pattern; from top to bottom, the layer distances exhibit a kind of oscillatory behavior around the uniform distance of 2, starting with smaller distance between the layers compared to the uniform case. A similar pattern can be observed for the random heterojunctions that minimize the transmission coefficient; however, in this case the initial layers of constant thickness have larger distances compared to the uniform case. In the right insets of subfigures (a) and (b) we use the correlation length $r_c = 1$ and sketch the heterostructures that maximize (a) and minimize (b) the transmission coefficients.

In Figure 11, we compare the maximum (a), (c) and minimum (b), (d) transmission coefficients with and without the constraint of constant total thickness. For constrained total thickness, we can obtain larger transmission at slightly larger values

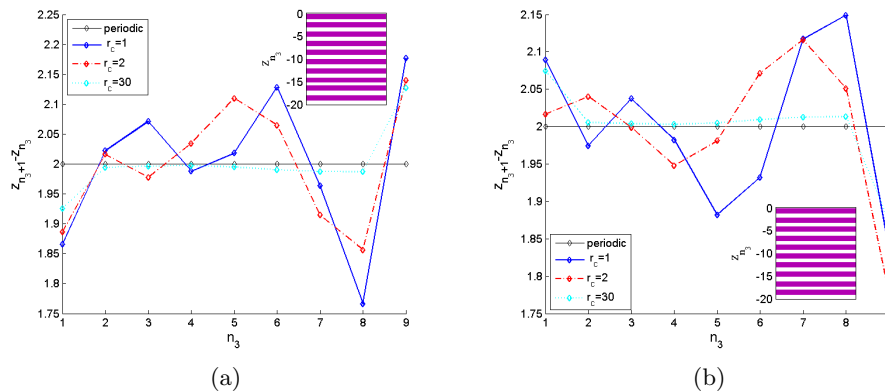


FIG. 10. In subfigures (a) and (b) the distances between the centers of layers of constant thickness that give the the transmission coefficient plotted in (a) and (b) of Figure 9, respectively, are shown. In the subfigures' right insets, realizations of the multilayered random structures with the distances plotted for $r_c = 1$ are shown. n_3 labels the layer along the z -direction.

of the wave number k_ρ of the incoming wave. On the other hand, in Figure 12 we show that for a different value of the shape parameter and with the constant total thickness the peaks of the transmission coefficient are shifted to lower values of k_ρ .

5.3. Random MMs that maximize and minimize the transmission coefficients. In this section, we will apply our methodology to 3-D MMs using a volume integral equation method for Maxwell equations [4] having high-dimensional random inputs from the ME-PCM with SGs [7]. In MM design for solar cell applications, of interest is the maximization of the reflection or the transmission coefficient within a range of frequency ω and the angle of incidence φ of the incoming radiation in the x - z plane. Here we examine the effect of the random perturbations of the positions of the cubic meta-atoms on the reflection coefficient for different angles of incidence $\varphi \in [0, \frac{\pi}{2}]$ while keeping the frequency constant at $\omega = 2$. The permeability of the random cubes is $\mu = 1$, and the change in dielectric constant of the cubes with respect to the background dielectrics is $\Delta\epsilon = 4$. More details about the deterministic solver can be found in [4].

Let R_{max} and R_{min} be the reflection coefficients of some optimized structure corresponding to the realizations $\theta_{max}, \theta_{min}$, which are defined by

$$(49) \quad R_{max}(\eta_1, r_c) = R_{max}(\theta_{max}, \eta_1, r_c),$$

where θ_{max} is given by

$$(50) \quad IR_{max}(\theta_{max}, \eta_1, r_c) = \max_{\theta \in \Theta} \int_0^{\frac{\pi}{2}} R(\theta, \eta_1, r_c, \varphi) d\varphi,$$

and $R_{min}(\eta_1, r_c)$ is defined similarly. In the following examples, the length of the cube size is set as $l = 0.5$ and the initial distances between the cubes in each direction are set equal to each other, i.e., $\alpha = b = c = 0.6111$.

Let us first consider a meta-surface consisting of 10×10 cubes on the xy -plane. The centers of the cubes are initially uniformly spaced inside the square $[-5, 5] \times [-5, 5]$. In the x -direction we assume random perturbations follow an SSRF covariance function with a damped oscillatory profile for $\eta_1 = -1.9$ and different values of

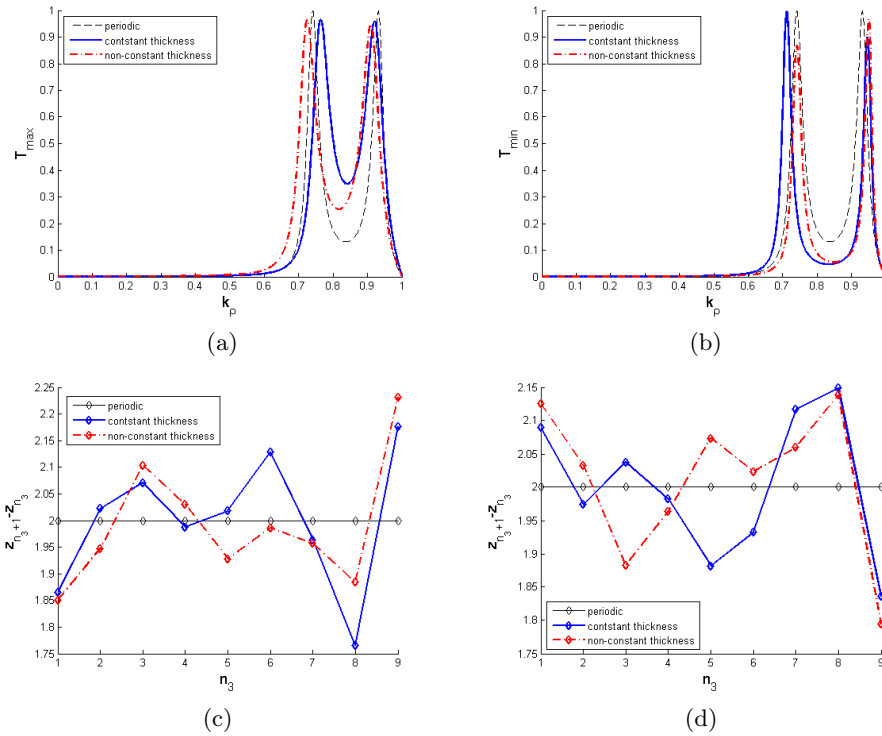


FIG. 11. Comparison of maximum (a) and minimum (b) of the transmission coefficient for different k_p with respect to whether we consider the constraint of constant total thickness. In sub-figures (c), (d) we display random distances between the centers of layers of constant thickness corresponding to (a), (b). n_3 labels the layer along the z -direction.

the correlation length $r_{cx} = 1.5, 2, 3$. In the y -direction we assume random perturbations follow the modified exponential covariance for $\eta_1 = 2$ and constant correlation length $r_{cy} = 3$. We truncate the K-L basis by using four and three random dimensions in the x - and y -directions, respectively, capturing more than 90% of the energy. In each random dimension we use two collocation points and thus 128 sampling points based on a tensor-product rule. For the most correlated case we will also discuss results for a higher resolution in the probability space using level 3 SGs, with $2^3 - 1$ collocation points, in combination with the MEPCM. We depict the results obtained by SGs using cross markers in the figures that follow. In this section we follow the continuous-discrete approach of the presented methodology. In Figure 13 we compare the maximum and minimum relative increases of the reflection coefficient for different values of the correlation length for nine different incident angles. In Figures 14 and 15 we plot the distances between the centers of the cubes in the x - and y -directions, respectively, corresponding to the cubes' surfaces that maximize (minimize) the reflection. We can see that the maximum (minimum) reflection coefficient decreases (increases) with the correlation length. The surfaces that maximize (minimize) the reflection coefficient follow a similar pattern; from left to right, the layer distances exhibit a kind of oscillatory behavior around the uniform distance of 1.1116, ending with a decreased (increased) distance between the cubes in the x -direction. We notice that for smaller correlation lengths the oscillations have higher frequencies and

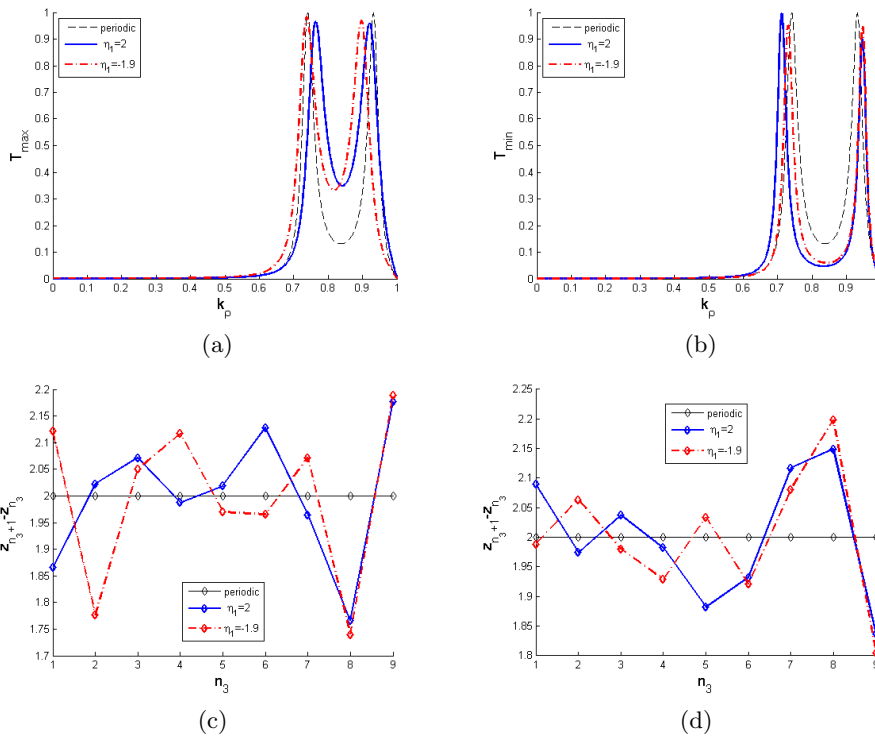


FIG. 12. Comparison of maximum (a) and minimum (b) of the transmission coefficient for different k_p with respect to the shape parameter η_1 of the SSRF model. In subfigures (c), (d) we display random distances between the centers of layers of constant thickness corresponding to (a), (b). n_3 labels the layer along the z -direction.

are shifted to the right. Higher frequencies are expected since for smaller correlation lengths the oscillations of the continuous sample paths also exhibit higher frequencies. In the y -direction the oscillation that maximizes the reflection ends with an increased distance of the cubes compared to the uniform case. Also, y -direction oscillation is not affected by the different values of $r_{cx} = 1.5, 2, 3$, while $r_{cy} = 3$ remains constant. The latter may change if nonseparable covariances were considered. For higher resolution in the probability space (260 sampling points by applying level 3 SGs with the MEPCM), the mean value and the variance of the reflection coefficient exhibit an absolute error less than 0.005% with respect to tensor product sampling for two collocation points indicating convergence in the mean square sense. The maximum relative reflection obtained by the 260 sampling points follows similar trends in Figure 13 for $r_{cx} = 1.5$ with a 2% decrease for the angle $\varphi = 1.5708$. The surfaces that maximize the reflection in Figure 14 follow similar patterns in the x -direction, while they keep the initial uniform distance positions in the y -direction in Figure 15. The latter indicates that for the 2-D MM the reflection coefficient is more sensitive to the perturbations in the x -direction.

Next, we consider a 3-D MM consisting of $10 \times 3 \times 3$ cubes in the xyz -space. The centers of the cubes are initially uniformly distributed inside the box $[-5, 5] \times [0, 2.222] \times [0, 2.222]$. In the x -direction we assume random perturbations follow an SSRF covariance function with a damped oscillatory profile close to the permissibility

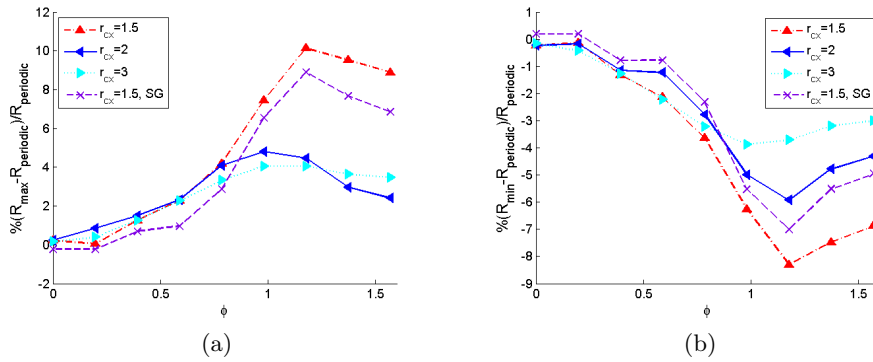


FIG. 13. (a) Maximum relative reflection coefficients increase for a 100-cube surface for different correlation lengths r_{cx} , constant frequency, and different angles of incidence. (b) Minimum relative reflection coefficients increase.

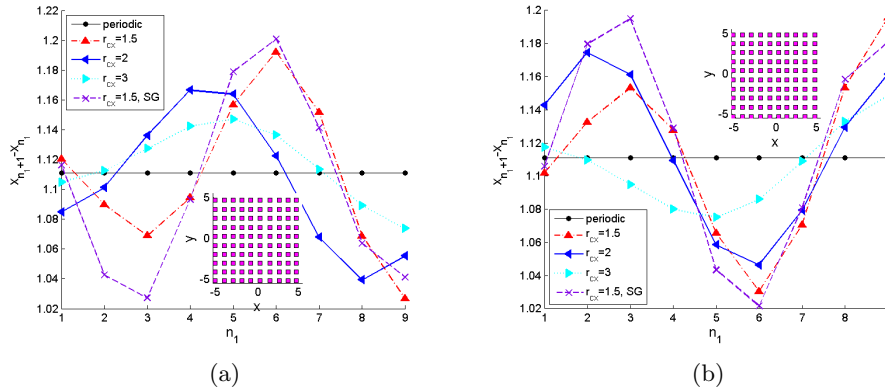


FIG. 14. In subfigures (a) and (b) the distances between the centers of the cubes in the x -direction that give the reflection coefficient plotted in (a) and (b) of Figure 13, respectively, are shown. In the subfigures' insets, realizations of the random surfaces with the distances plotted for $r_c = 1.5$ are shown. n_1 labels the meta-atoms along the x -direction.

boundary for $\eta_1 = -1.987$ and with $r_{cx} = 1.5, 2, 3$. In the y - and z -directions we assume random perturbations follow the modified exponential covariance for $\eta_1 = 2$ and constant correlation lengths $r_{cy} = r_{cz} = 1.5$. We truncate the K-L basis by keeping three random dimensions in the x - and two random dimensions in each of the y - and z -directions, capturing more than 90% of the energy for this choice of the shape parameters η_1 . For $r_{cx} = 2$ we consider the same two levels of resolution in the probability space as for the 2-D surface discussed above.

In Figure 16 we compare the maximum (a) and minimum (b) relative increases of the reflection coefficient obtained for the different values of the correlation length for nine different angles of incidence.

In Figures 17, 18, and 19 we plot the distances between the centers of the cubes in the x -, y -, and z -directions, respectively, corresponding to the cubes' surfaces that maximize the reflection. In the y - and z -directions, the monotonic increase (decrease) of the distances is the result of allowing only three degrees of freedom for the cubes' positions due to our initial grid size selection. Nevertheless, the changes of the distance

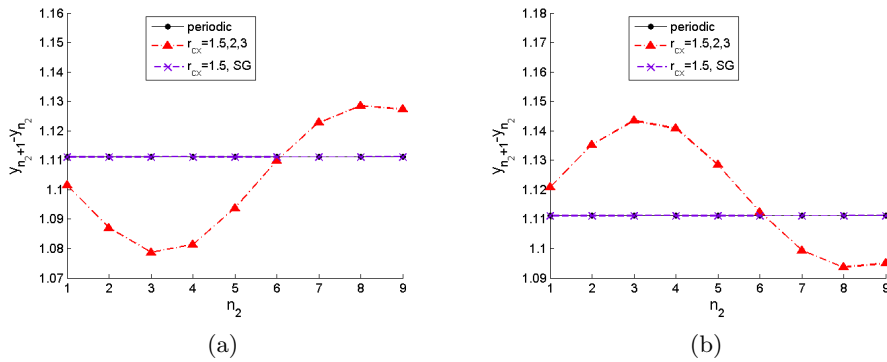


FIG. 15. In subfigures (a) and (b) the distances between the centers of the cubes in the y -direction that give the reflection coefficient plotted in (a) and (b) of Figure 13, respectively, are shown. n_2 labels the meta-atoms along the y -direction.

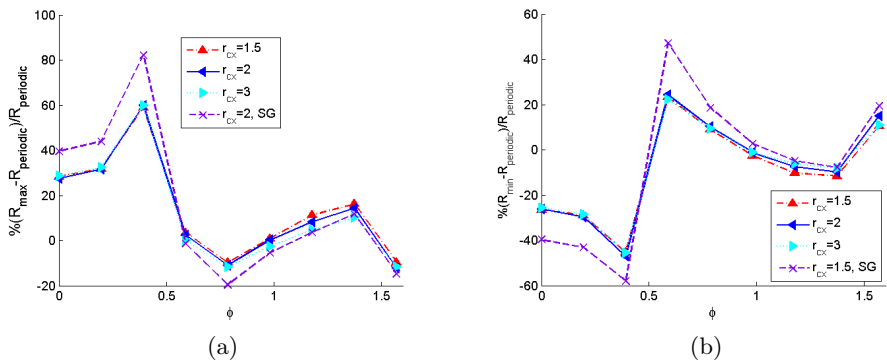


FIG. 16. (a) Maximum relative reflection coefficients increase for a 90-cube 3-D surface for different correlation lengths r_{cx} , constant frequency, and different angles of incidence. (b) Minimum relative reflection coefficients increase.

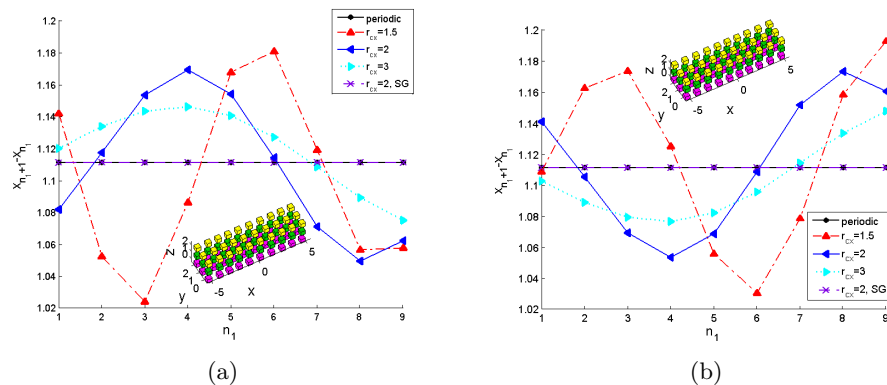


FIG. 17. In subfigures (a) and (b) the distances between the centers of the cubes in the x -direction that give the reflection coefficient plotted in (a) and (b) of Figure 16, respectively, are shown. In the subfigures' insets, realizations of the random surfaces with the distances plotted for $r_c = 1.5$ are shown. n_1 labels the meta-atoms along the x -direction.

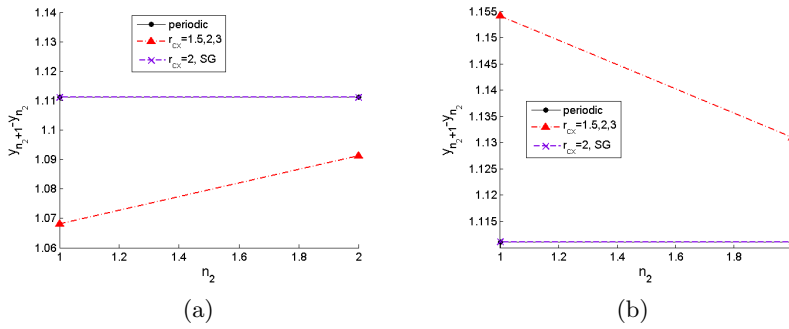


FIG. 18. In subfigures (a) and (b) the distances between the centers of the cubes in the y -direction that give the reflection coefficient plotted in (a) and (b) of Figure 16, respectively, are shown. n_2 labels the meta-atoms along the y -direction.

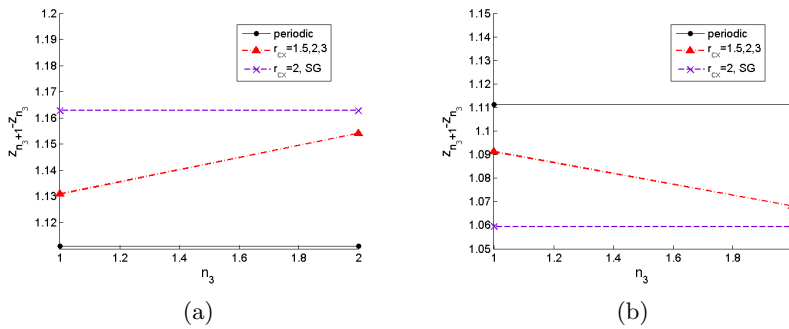


FIG. 19. In subfigures (a) and (b) the distances between the centers of the cubes in the z -direction that give the reflection coefficient plotted in (a) and (b) of Figure 16, respectively, are shown. n_3 labels the meta-atoms along the z -direction.

in the x - and y -directions obtained by the tensor product sampling in Figures 17 and 18 (triangle markers) follow patterns similar to those plotted in Figures 14 and 15 for the optimized surface. Moreover, the random perturbations of 3-D MM resulted in a 10% relative increase of the reflection coefficient for $\varphi = 1.178$ and $r_{cx} = 1.5$, which is similar to the meta-surface case in Figure 16. However, the relative increase of the reflection of the optimized configuration in 3-D goes to 60% from 2% when $\varphi = 0.3927$ for all the different values of the correlation lengths r_{cx} . The latter indicates that the reflection is more sensitive to the perturbations in the other directions. For the higher resolution in the probability space, the reflection of the optimized configuration (purple cross in Figure 16) reaches 82.2% for $\varphi = 0.3927$ with a simultaneous decrease for $\varphi = 0.7854$ compared with the lower resolution case. The optimal MM in Figures 18 and 19 is obtained following perturbations only in the z -direction.

Finally, we consider a 3-D MM consisting of $5 \times 5 \times 5$ cubes uniformly distributed in the box $[0, 4.444] \times [0, 4.444] \times [0, 4.444]$. In the x -, y - and z - directions we assume random perturbations follow an SSRF covariance function with a damped oscillatory profile for $\eta_1 = -1.9$ and with $r_{cx} = r_{cy} = r_{cz} = 1.5, 2, 3$. We truncate the K-L basis by keeping four random dimensions in each direction capturing more than 98% of the total energy. We use the level 2 sparse grid in combination with the MEPCM to find the configuration that maximizes the reflection out of 37 samples. In

Figure 20(a) we compare the maximum relative increase of the reflection coefficient obtained for the different values of the correlation length for nine different angles of incidence. As we can see for $\varphi = 0$ the relative increase reaches 43% and is sensitive to the correlation length. In Figure 20(b) we plot the distance between the centers of the cubes in the z -direction, corresponding to the cubes' surfaces that maximize the reflection. The fact that the maximum reflection results from the perturbation in the z -direction is in agreement with the previous observation, and thus we can conclude that in the considered 3-D cases the reflection coefficient is more sensitive to the random perturbations in the z -direction. However, the sensitivity may vary for different angles and different frequencies of the incoming wave. In future work, we shall use the adaptive ANOVA decomposition and the Sobol' sensitivity indexes [29] to further investigate the sensitivity of the reflection coefficient to different parameters as well as how to deal with dimensionality challenges arising for small correlation lengths.

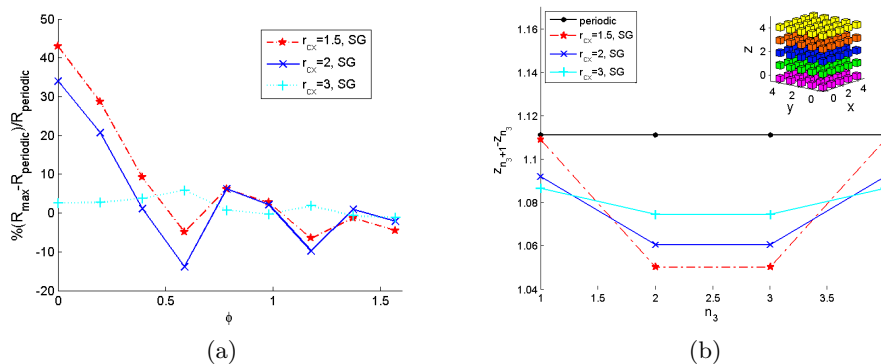


FIG. 20. In subfigure (a), the maximum relative increase of the reflection coefficient for a 125-cube surface for different correlation lengths, constant frequency, and different angles of incidence. In (b) the distances between the centers of the cubes in the z -direction that give the reflection coefficient plotted in (a) are shown. In the inset of subfigure (b), realizations of the random surfaces with the distances plotted for $r_{cx} = r_{cy} = r_{cz} = 1.5$ are shown.

6. Summary and discussion. In this paper, we have developed a general computational stochastic methodology to model the effects of randomness in the relative positions of meta-atoms on optical properties of MMs. We have constructed continuous and discrete RFs with given probabilistic characteristics. We project the RFs onto a uniform reference mesh to create samples of random configurations of the meta-atoms' positions. The correlated random meta-atoms we have obtained satisfy the geometric volume exclusion constraint as well as the entropic "clothes-pin" effect. We have used RFs with covariance from the Spartan family, which includes the modified exponential as well as damped oscillatory covariance functions whose random samples can exhibit an almost oscillatory behavior.

The proposed algorithms were applied to explore the effects of randomness in the electromagnetic wave propagation through multilayered heterojunctions and 3-D MMs with different dielectric constants and random spacing. The wave scattering is solved by the transfer and scattering matrices method for the heterojunctions or by a 3-D Nystrom volume integral method for the 3-D MMs. The mean and the variance of the transmission coefficients for different correlations of the random configurations are obtained, which show that for short-range correlations the transmission coefficients

exhibit larger variances. This finding indicates that these configurations can be used to obtain MMs with optimized properties. In fact, optimized configurations of the heterojunctions and 3-D MMs were found that led to larger or smaller transmission coefficients for different wave numbers of the incoming wave and different correlations. The maximum (minimum) transmission was achieved for a configuration with an oscillatory spacing profile along the propagation direction. In addition, short-range correlations in the material lead to higher values of the transmission coefficient for a broader range of wave numbers compared to the periodic structure. Moreover, we found that for certain configurations of the material with damped oscillatory covariance we were able to shift the peaks of the optimized coefficients to lower wave numbers. Finally, we found out that the vertical direction in 3-D MMs offers more possibilities in achieving larger enhancement of optical properties.

Acknowledgment. I. C. Tsantili would like to thank Prof. D. T. Hristopulos for discussions on the continuum RFs and the implementation of the algorithm.

REFERENCES

- [1] M. ABRAMOWITZ AND I. A. STEGUN, *Handbook of Mathematical Functions: With Formulas, Graphs, and Mathematical Tables*, National Bureau of Standards Applied Mathematics Series 55, U.S. Government Printing Office, Washington, D.C., 1964.
- [2] S. BOCHNER, *Lectures on Fourier Integrals*, Princeton University Press, Princeton, NJ, 1959.
- [3] W. CAI, *Computational Methods for Electromagnetic Phenomena: Electrostatics in Solvation, Scattering, and Electron Transport*, Cambridge University Press, Cambridge, UK, 2013.
- [4] D. CHEN, W. CAI, B. ZINSER, AND M. H. CHO, *Accurate and efficient Nyström volume integral equation method for the Maxwell equations for multiple 3-d scatterers*, J. Comput. Phys., 321 (2016), pp. 303–320, <https://doi.org/10.1016/j.jcp.2016.05.042>.
- [5] M. H. CHO AND W. CAI, *A parallel fast algorithm for computing the Helmholtz integral operator in 3-d layered media*, J. Comput. Phys., 231 (2012), pp. 5910–5925, <https://doi.org/10.1016/j.jcp.2012.05.022>.
- [6] V. E. FERRY, M. A. VERSCHUREN, M. C. V. LARE, R. E. SCHROPP, H. A. ATWATER, AND A. POLMAN, *Optimized spatial correlations for broadband light trapping nanopatterns in high efficiency ultrathin film a-si:H solar cells*, Nano Lett., 11 (2011), pp. 4239–4245, <https://doi.org/10.1021/nl202226r>.
- [7] J. FOO AND G. E. KARNIADAKIS, *Multi-element probabilistic collocation method in high dimensions*, J. Comput. Phys., 229 (2010), pp. 1536–1557, <https://doi.org/10.1016/j.jcp.2009.10.043>.
- [8] R. G. GHANEM AND P. D. SPANOS, *Stochastic Finite Elements: A Spectral Approach*, revised ed., Dover, New York, 2003.
- [9] D. T. HRISTOPULOS, *Spartan Gibbs random field models for geostatistical applications*, SIAM J. Sci. Comput., 24 (2003), pp. 2125–2162, <https://doi.org/10.1137/S106482750240265X>.
- [10] D. T. HRISTOPULOS, *Covariance functions motivated by spatial random field models with local interactions*, Stochastic Environ. Res. Risk Assess., 29 (2015), pp. 739–754, <https://doi.org/10.1007/s00477-014-0933-0>.
- [11] D. T. HRISTOPULOS AND S. N. ELOGNE, *Analytic properties and covariance functions for a new class of generalized Gibbs random fields*, IEEE Trans. Inform. Theory, 53 (2007), pp. 4667–4679, <https://doi.org/10.1109/TIT.2007.909163>.
- [12] D. T. HRISTOPULOS AND E. PORCU, *Multivariate Spartan spatial random field models*, Probab. Eng. Mech., 37 (2014), pp. 84–92, <https://doi.org/10.1016/j.probengmech.2014.06.005>.
- [13] D. T. HRISTOPULOS AND I. C. TSANTILI, *Space-time models based on random fields with local interactions*, Internat. J. Modern Phys. B, 30 (2016), 1541007, <https://doi.org/10.1142/S0217979215410076>.
- [14] D. T. HRISTOPULOS AND M. ŽUKOVIČ, *Relationships between correlation lengths and integral scales for covariance models with more than two parameters*, Stochastic Environ. Res. Risk Assess., 25 (2011), pp. 11–19, <https://doi.org/10.1007/s00477-010-0407-y>.
- [15] D. Y. K. KO AND J. R. SAMBLES, *Scattering matrix method for propagation of radiation in stratified media: Attenuated total reflection studies of liquid crystals*, J. Opt. Soc. Amer. A, 5 (1988), pp. 1863–1866, <https://doi.org/10.1364/JOSAA.5.001863>.

- [16] W. KRAUTH, *Statistical Mechanics: Algorithms and Computations*, Oxf. Master Ser. Phys. 13, Oxford University Press, Oxford, UK, 2006.
- [17] M. LOÈVE, *Probability Theory*, Springer-Verlag, New York, 1978.
- [18] B. MATÉRN, *Spatial Variation*, Lect. Notes Stat. 36, Springer Science & Business Media, Berlin, Heidelberg, 2013.
- [19] A. POLMAN AND H. A. ATWATER, *Photonic design principles for ultrahigh-efficiency photovoltaics*, Nat. Mater., 11 (2012), pp. 174–177, <https://doi.org/10.1038/nmat3263>.
- [20] F. RIBOLI, P. BARTHELEMY, S. VIGNOLINI, F. INTONTI, A. DE ROSSI, S. COMBRIE, AND D. S. WIERSMA, *Anderson localization of near-visible light in two dimensions*, Opt. Lett., 36 (2011), pp. 127–129, <https://doi.org/10.1364/OL.36.000127>.
- [21] P. D. SPANOS, M. BEER, AND J. RED-HORSE, *Karhunen–Loève expansion of stochastic processes with a modified exponential covariance kernel*, J. Eng. Mech., 133 (2007), pp. 773–779, [https://doi.org/10.1061/\(ASCE\)0733-9399\(2007\)133:7\(773\)](https://doi.org/10.1061/(ASCE)0733-9399(2007)133:7(773)).
- [22] I. C. TSANTILI AND D. T. HRISTOPOULOS, *Karhunen–Loève expansion of Spartan spatial random fields*, Probab. Eng. Mech., 43 (2016), pp. 132–147, <https://doi.org/10.1016/j.proengmech.2015.12.002>.
- [23] K. VYNCK, M. BURRESI, F. RIBOLI, AND D. S. WIERSMA, *Photon management in two-dimensional disordered media*, Nat. Mater., 11 (2012), pp. 1017–1022, <https://doi.org/10.1038/nmat3442>.
- [24] D. S. WIERSMA, *Disordered photonics*, Nat. Photonics, 7 (2013), pp. 188–196, <https://doi.org/10.1038/nphoton.2013.29>.
- [25] D. XIU AND J. S. HESTHAVEN, *High-order collocation methods for differential equations with random inputs*, SIAM J. Sci. Comput., 27 (2005), pp. 1118–1139, <https://doi.org/10.1137/040615201>.
- [26] D. XIU AND G. E. KARNIADAKIS, *The Wiener–Aaskey polynomial chaos for stochastic differential equations*, SIAM J. Sci. Comput., 24 (2002), pp. 619–644, <https://doi.org/10.1137/S1064827501387826>.
- [27] A. M. YAGLOM, *Correlation Theory of Stationary and Related Random Functions. Volume I: Basic Results*, Springer-Verlag, New York, 1987.
- [28] X. YANG, M. CHOI, AND G. E. KARNIADAKIS, *MEPCMP version 1.01*, <https://sourceforge.net/projects/mepcpackage/>, 2011–2012.
- [29] X. YANG, M. CHOI, G. LIN, AND G. E. KARNIADAKIS, *Adaptive ANOVA decomposition of stochastic incompressible and compressible flows*, J. Comput. Phys., 231 (2012), pp. 1587–1614, <https://doi.org/10.1016/j.jcp.2011.10.028>.